(Received 21 February 2024, Accepted 27 April 2024, Scheduled 7 May 2024)

Simulation Study of Digital Spatial Processing in Conditions of Tropospheric Propagation of Radio Waves for Telecommunication Applications

Ilia Peshkov*

Department of Physics, Radio Engineering and Electronics, Bunin Yelets State University, Russia

ABSTRACT: In this paper, the propagation of electromagnetic rays in a tropospheric waveguide and spatial processing using digital antenna arrays are studied. The beam traveling through the layers of the atmosphere depends on the refractive index and its vertical change. In this regard, conditions may arise when radio rays propagate in a waveguide manner at low altitudes. In this case, attenuation takes place, and the effect of multipath fading may also occur, when several rays reflected from different layers of the troposphere and with various spatial coordinates in elevation arrive at the receiver. It is proposed to apply digital antenna arrays to increase the range and reliability of radio communication through the tropospheric waveguide. Parabolic equations are utilized to estimate the path loses of radio waves of the centimeter wavelength. A ray-tracing algorithm via a tropospheric waveguide is used to estimate the mutual phases in the aperture of the receiving array. Bit error rate curves were obtained depending on the geometry of the antenna arrays after the signal passed through the tropospheric waveguide.

1. INTRODUCTION

The atmospheric refraction of radiation from any telecommunication system causes it to bend towards the Earth's surface in one or another way [1]. Refraction is caused by a (gradual or hopping) decrease in the real part of the refractive index of air from values of 0.1 at the surface to 1 in outer space. In this case, signals of centimeter wavelengths can reach the receiving terminals several hundred kilometers from the transmitter [2–4].

Presently, a considerable number of publications are devoted to the investigation and simulation of the propagation of radio waves through a tropospheric duct. As a rule, they investigate the problem from only one side. Either attenuation is studied [5, 6], or consideration is taken from the point of view of the ray-tracing algorithm [7–11]. The main idea of the paper is to combine both of these approaches for modeling antenna arrays with directional elements and digital spatial processing. In addition, the paper simulates a tropospheric waveguide with a random refraction coefficient.

The use of digital antenna arrays is being investigated to overcome the challenges of establishing this type of communication, such as high attenuation and weather conditions [12]. At the initial stage, attenuation is estimated by means of parabolic equations, and then the propagation path is calculated using a ray-tracing algorithm from the transmitter to the receiving digital antenna array. At the last stage, the modeling of spatial processing algorithms is carried out (the direction-of-arrival estimation, as well as digital beamforming) with the calculation of the probability of a bit error rate depending on the geometry of the antenna array.

2. REFRACTIVE INDEX OF RADIO SIGNALS

The real part of the refractive index can be expressed as a function of atmospheric pressure, humidity, and air temperature. The formula of the index is semi-empirical and can be written as [13]:

$$n = 1 + 77.6 \times 10^{-6} \frac{P}{T} + 0.373 \frac{e}{T^2} \tag{1}$$

where P is the atmospheric pressure in millibars, T the temperature in degrees Kelvin, and e the water vapor pressure in millibars. Equation (1) is known as the Debye formula, and it has been shown to have an accuracy of $\pm 0.5\%$ [3]. The refractive index n rarely exceeds 1.0004 on the surface, and it is advisable to introduce the so-called radiorefraction N, defined as:

$$N = (n - 1) \times 10^6 \tag{2}$$

The propagation of radio waves depends more on the refractive gradients than on the value of N itself [2]. As a rule, noticeable refractive gradients in the horizontal direction occur on a much larger scale (tens of meters to tens of kilometers) than in the vertical direction (tens of meters to hundreds of meters). Hence, it is commonly assumed that the atmosphere exhibits a horizontal stratification. Consequently, in the subsequent analysis, solely the altitude-dependent refraction is taken into account, disregarding any horizontal variations.

* Corresponding author: Ilia Peshkov (ilvpeshkov@gmail.com).

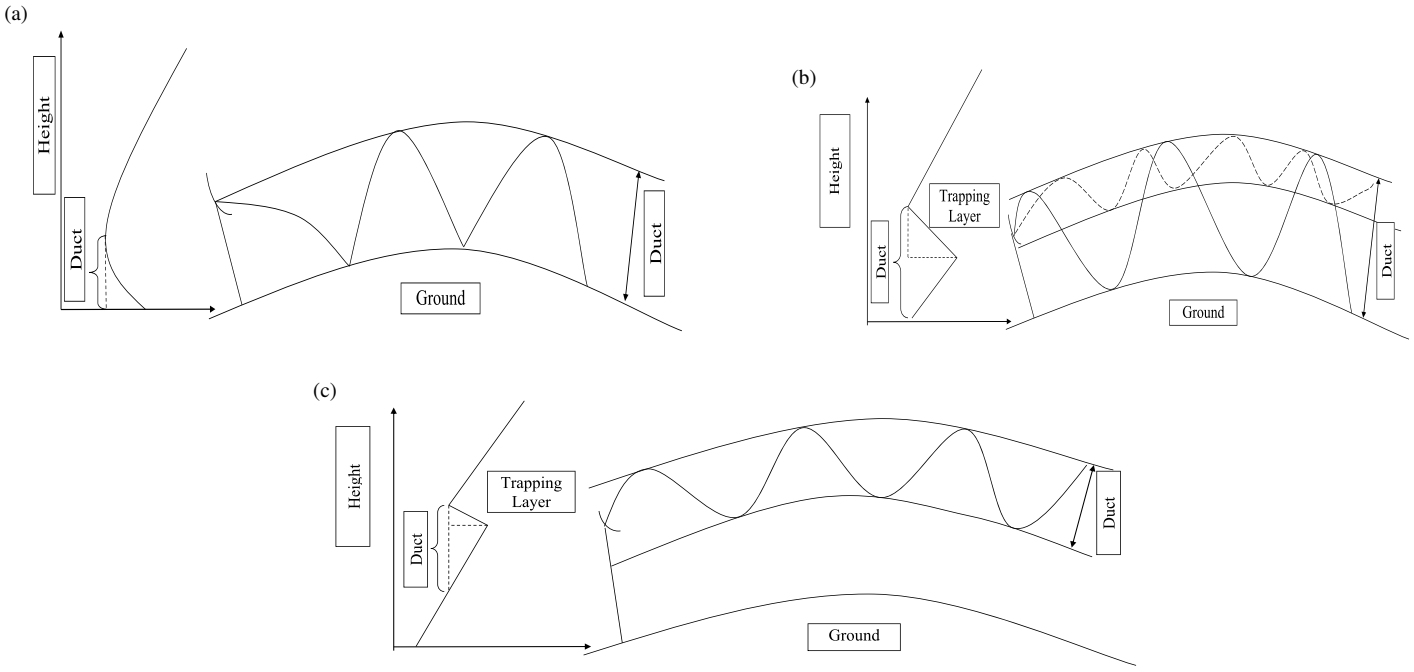

FIGURE 1. M-profiles as function of altitude: (a) simple surface duct, (b) surface S-shaped duct, (c) elevated duct.

In the same way, in order to include the curvature of the Earth, the modified refraction M is determined from the modified refractive index m as follows [14]:

$$M = (m-1)\times 10^6 = 10^6 \times \left(n - 1 + \frac{z}{R_E}\right) = N + 10^6 \times \frac{z}{R_E} \quad (3)$$

where R_E is the radius of the earth, and z is the vertical coordinate or the altitude.

The surface and elevated air ducts are modeled by a three-line curve, as depicted in Fig. 1. The case in Fig. 1(a) illustrates the structure associated with a simple surface channel. In Fig. 1(b), a surface S-shaped duct reaching the surface is depicted, but the trapping layer does not. In these two cases, the channel thickness is the height difference between the ground and the upper part of the duct, where the minimum of the changed refraction profile is achieved. The elevated channel is shown in Fig. 1(c) [5].

As mentioned above, the duct is the result of strong vertical changes in the refractive index of the atmosphere between air masses of different temperatures and humidity, especially at low atmospheric levels. Thus, the tropospheric waveguide allows over-the-horizon long-range radio communication.

3. THE PARABOLIC EQUATION

The parabolic equation for tropospheric propagation problems was first introduced by Leontovich and Fok in 1946 [15] and has been gradually improved since then.

The field component (electric or magnetic) ϕ satisfies:

$$\frac{\partial^2\phi}{\partial x^2} + \frac{\partial^2\phi}{\partial z^2} + k^2 n^2 \phi = 0 \quad (4)$$

here k is the wave number of free space, and ϕ is either E_y or H_y for horizontal or vertical field polarization, respectively. The so-called reduced function $u(x,z)$ is introduced as follows:

$$u(x,z) = e^{-kx}\phi(x,z) \quad (5)$$

where x is the coordinate.

The point of doing this substitution and solving for $u(x,z)$ instead of $\phi(x,z)$ is that $u(x,z)$ now slowly changes depending on the direction of propagation. With this substitution, the scalar wave Equation (4) takes the form:

$$\left\{\frac{\partial^2}{\partial x^2} + \frac{\partial^2}{\partial z^2} + 2ik\frac{\partial}{\partial x} + k^2\left[n^2 - 1\right]\right\} u(x,z) = 0 \quad (6)$$

This equation is still classified as elliptical rather than parabolic. It is customary to introduce a pseudodifferential operator $Q = \sqrt{\frac{1}{k^2}\frac{\partial^2}{\partial z^2} + n^2} = \sqrt{1+q}, \quad q = \frac{1}{k^2}\frac{\partial^2}{\partial z^2} + (n(x,z) - 1)$ and factorize Equation (3). Thanks to this substitution, the deducing becomes more general [12]:

$$\left\{\frac{\partial}{\partial x} + ik(1-Q)\right\}\left\{\frac{\partial}{\partial x} + ik(1+Q)\right\} u = 0 \quad (7)$$

Now, divide Equation (7) into one part propagating forward (positive direction x) and another part propagating in the opposite direction:

$$\frac{\partial u}{\partial x} = -ik(1-Q)u \quad (8)$$

$$\frac{\partial u}{\partial x} = -ik(1+Q)u \quad (9)$$

The simultaneous solution of both forward and reverse traveling waves is obtained in [16]:

$$u(x,z) = Ae^{ikx(Q-1)}, \quad (10)$$

where A is the amplitude of the wave.

If the initial reduced field $u(0,z)$ is known, Equation (10) is simply repeated in increments of Δx until the desired range is reached [17]:

$$u\left(x+\Delta x,z\right)=e^{ik\Delta x(Q-1)}u\left(x,z\right) \tag{11}$$

In order to actually solve Equation (8) in practice, Q must be approximated in such a way that it can be solved using standard algorithms. Then, the accuracy of the resulting parabolic equation is directly related to the form Q, which will be shown below. There are various methods for solving Equation (8). The most common methods found in the existing literature are the Fourier transform split-step parabolic equation methods, finite element methods, and finite difference methods [18].

After calculating the field strength according to (11), it is necessary to estimate the attenuation on the link, for which the propagation and loss coefficients are utilized. The propagation factor (*PF*, dB) is defined as the square of the ratio of the amplitude of the electric field at a given point under certain conditions to the amplitude of the electric field obtained at the same point under conditions of free propagation. Formula (20) gives an expression of the propagation factor of the parabolic equation field $u(x,z)$, as well as a relationship with the amount of losses on the link, (*PL*, dB) [19]:

$$PF=20\log\left|u\left(x,z\right)\right|+10\log\left(r\right)+10\log\left(\lambda\right) \tag{12}$$

$$PL=20\log\left(\frac{4\pi r}{\lambda}\right)-PF \tag{13}$$

where λ is the wavelength, and r is the range.

4. RAY TRACING USING A SECOND-ORDER ORDINARY DIFFERENTIAL EQUATION

In order to simulate the antenna arrays with directional elements and spatial filtering of signals which are traveled via tropospheric waveguides, ray tracing algorithm is necessary. Several algorithms have been proposed, such as [5, 7, 19–21]. Many of them [6, 19–21] have the drawback that the layers of the atmosphere are considered piecewise, linearly, whereas the process of ray propagation is continuous. This feature is used in differentiation [7], which is taken in the case of antenna arrays.

From differential geometry (Fig. 2) it is possible to obtain for infinitesimal *dh* and *dr* [7]:

$$\sin e=\frac{dh}{dr} \tag{14}$$

$$\cos e=\sqrt{1-\left(\frac{dh}{dr}\right)^2}\left(\geq 0,\text{ i.e., }e\in\left[-\frac{\pi}{2},\frac{\pi}{2}\right]\right) \tag{15}$$

Then

$$nh\left(r\right)\left[R_E+h\left(r\right)\right]\sqrt{1-\left(\frac{dh}{dr}\right)^2}=\text{const} \tag{16}$$

As indicated, it is assumed that h is a function of r, so the refractive index of n is implicitly dependent on r. Equation (18)

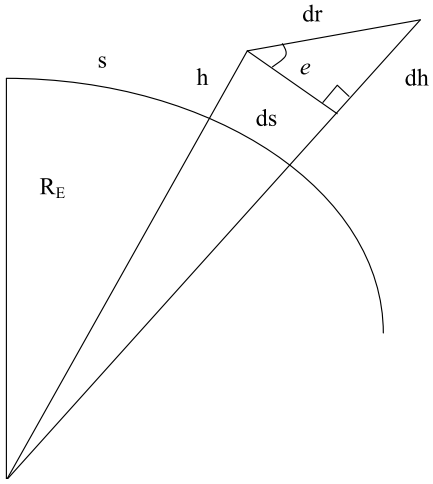

FIGURE 2. Sketch of R_E, h, and their differentials for the derivation of the ray tracing algorithm.

is differentiated by r and obtained as follows:

$$\frac{dn}{dh}\frac{dh}{dr}\left(R_E+1\right)\sqrt{1-\left(\frac{dh}{dr}\right)^2}+n\frac{dh}{dr}\sqrt{1-\left(\frac{dh}{dr}\right)^2}$$

$$+n\left(R_E+1\right)\frac{-2\frac{dh}{dr}\frac{d^2h}{dr^2}}{2\sqrt{1-\left(\frac{dh}{dr}\right)^2}}=0 \tag{17}$$

Singularities $\frac{dh}{dr}=\pm1$ can be deleted by multiplying by $\sqrt{1-\left(\frac{dh}{dr}\right)^2}$, which gives:

$$\frac{dh}{dr}\left\{n\left(R_E+1\right)\frac{d^2h}{dr^2}+\left(\frac{dh}{dr}\right)^2\left[\frac{dn}{dh}\left(R_E+1\right)+n\right]\right.$$

$$\left.-\left[\frac{dn}{dh}\left(R_E+1\right)+n\right]\right\}=0 \tag{18}$$

Because $\frac{dh}{dr}=0$ is unphysical, as a general solution, it is argued that:

$$n\left(R_E+1\right)\frac{d^2h}{dr^2}+\left(\frac{dh}{dr}\right)^2\left[\frac{dn}{dh}\left(R_E+h\right)+n\right]$$

$$-\left[\frac{dn}{dh}\left(R_E+h\right)+n\right]=0 \tag{19}$$

Divide both parts of Equation (21) by $n(R_E+h)$ and obtain a nonlinear second-order ordinary differential equation (ODE):

$$\frac{d^2h}{dr^2}+\left(\frac{dh}{dr}\right)^2\left(\frac{1}{n}\frac{dn}{dh}+\frac{1}{R_E+h}\right)$$

$$-\left(\frac{1}{n}\frac{dn}{dh}+\frac{1}{R_E+h}\right)=0 \tag{20}$$

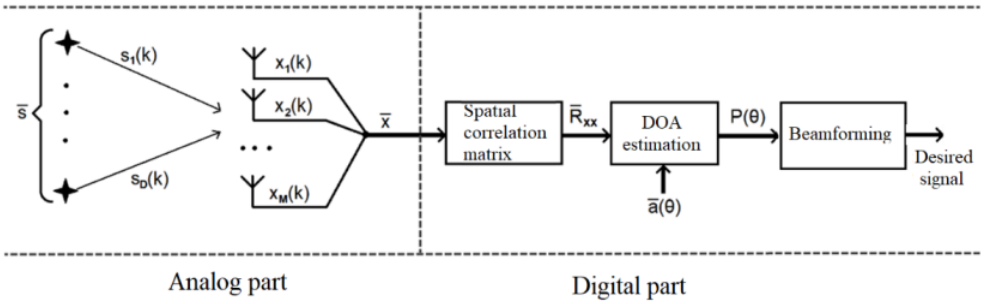

FIGURE 3. Common structure of digital antenna array.

and, replacing with $\frac{dh}{dr} = u$, an equivalent system of two related first-order equations will be obtained:

$$\frac{dh}{dr} = u \tag{21}$$

$$\frac{du}{dr} = -u^2\left(\frac{1}{n}\frac{dn}{dh} + \frac{1}{R_E + h}\right) + \left(\frac{1}{n}\frac{dn}{dh} + \frac{1}{R_E + h}\right) \tag{22}$$

Equations (23)–(24) can be considered as a problem with initial values:

$$u\left(r = 0\right) = \left.\frac{dh}{dr}\right|_{r=0} = \sin e_0 \tag{23}$$

$$h\left(r = 0\right) = h_0 \tag{24}$$

and the ray tracing problem is then uniquely solved by this ODE.

Equations (25)–(26) are solved in steps. The iteration step is performed as follows [7]:

Step 1: Estimate $\frac{1}{n_{l-1}}$ and $\left.\frac{dn}{dh}\right|_{l-1}$ at the height h_{l-1} using experimental data or approximate values.

Step 2: Solve Equations (24)–(25) with initial values u_{l-1} and h_{l-1}, to get u_l and h_l.

Step 3: Calculate the distance s_l according to the formula:

$$s_l = s_{l-1} + R_E \arcsin\left(\frac{\cos e_{l-1}\Delta r}{R_E + h_l}\right), \tag{25}$$

and also

$$e_l = \arcsin\left(u_{l-1}\right) \tag{26}$$

Steps 1–3 are repeated from $l = 1$ to $l = L$. The numerical differentiation in step 2 is implemented using the fourth-order Runge-Kutta method.

5. SIMULATION

The previous section of this article introduced methods for calculating the propagation of an electromagnetic beam in a stratified atmosphere. These received radio signals are summed in the aperture of the digital antenna array for subsequent spatial filtering shown in Fig. 3 [22].

Suppose that there is an antenna array consisting of M directional antenna elements. It receives D independent signals from different directions with angles θ (azimuth), φ (elevation), as shown in Fig. 3. Here $s_d(k)$ is the incident signal, $x_m(k)$ the received signal from the mth antenna element, and $y(k)$ the final output signal. As a result, the vector of the output signals has the following form:

$$\vec{\mathbf{x}} = \mathbf{A} \cdot \vec{\mathbf{s}} + \vec{\mathbf{n}} \tag{27}$$

where $\vec{\mathbf{n}}$ is the noise vector; $\mathbf{A}$ is the matrix of steering vectors:

$$\mathbf{A} = \left[\vec{\mathbf{a}}\left(\theta_1, \varphi_1\right) \;\; \vec{\mathbf{a}}\left(\theta_2, \varphi_2\right) \;\; \cdots \;\; \vec{\mathbf{a}}\left(\theta_D, \varphi_D\right)\right] \tag{28}$$

$$\vec{\mathbf{a}}(\theta, \phi) = \left[g_1(\theta, \phi)e^{jkr_1^T} \;\; g_2(\theta, \phi)e^{jkr_2^T} \;\; \cdots \;\; g_N(\theta, \phi)e^{jkr_N^T}\right] \tag{29}$$

where $\vec{\mathbf{k}} = \frac{2\pi}{\lambda}(k_x, k_y, k_z) = (\sin\varphi\cos\theta, \sin\varphi\sin\theta, \cos\varphi)$ is the wave vector; $\vec{\mathbf{r}}_n^T = (x_n, y_n, z_n)^T$ is the radius-vector to n-th antenna; and $g_n(\theta, \varphi)$ is the radiation pattern of the n-th antenna. Therefore, the steering vector of the antenna array can be expressed as follows:

$$\vec{\mathbf{a}}(\theta, \phi) = \begin{bmatrix} g_1(\theta - \theta_1, \varphi - \varphi_1)e^{j\vec{k}\vec{r}_1^T} \\ g_2(\theta - \theta_2, \varphi - \varphi_2)e^{j\vec{k}\vec{r}_2^T} \\ g_3(\theta - \theta_3, \varphi - \varphi_3)e^{j\vec{k}\vec{r}_3^T} \\ g_4(\theta - \theta_4, \varphi - \varphi_4)e^{j\vec{k}\vec{r}_4^T} \\ g_5(\theta - \theta_5, \varphi - \varphi_5)e^{j\vec{k}\vec{r}_5^T} \\ g_6(\theta - \theta_6, \varphi - \varphi_6)e^{j\vec{k}\vec{r}_6^T} \end{bmatrix} \tag{30}$$

The geometry of the receiving arrays is determined by the circular and hemispherical shape with directional antenna elements shown in Fig. 4, and a detailed description is provided below [23].

The antenna element has a directional pattern that is known and determined by the formula:

$$g_n\left(\varphi, \theta\right) = \frac{D}{2^{2m}}\left(1 + \sin\left(\varphi\right)\right)^m \left(1 + \cos\left(\theta - \frac{2\pi n}{N}\right)\right)^m, \tag{31}$$

where D is the coefficient of directional action, and m is determined by D.

The correlation matrix is determined by the following formula:

$$\hat{\mathbf{R}} = \frac{1}{K}\sum_{k=1}^{K} \vec{\mathbf{x}}(k)^H \vec{\mathbf{x}}(k) \tag{32}$$

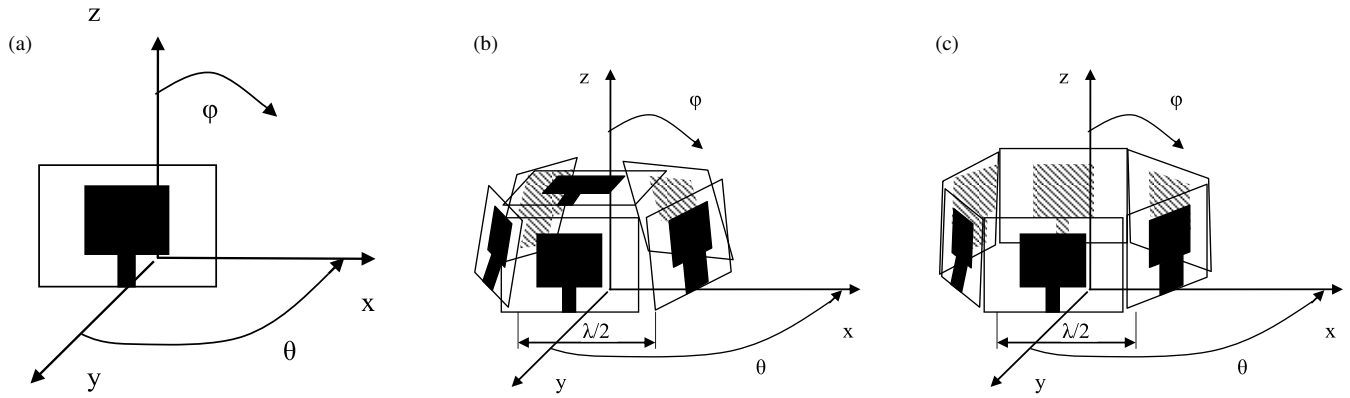

FIGURE 4. Antennas: (a) single, (b) hemispherical, (c) circular.

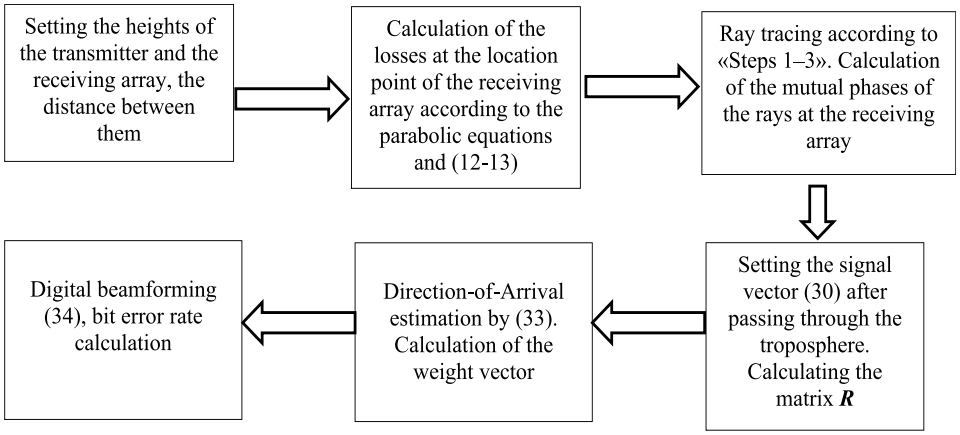

FIGURE 5. Generalized scheme for simulation.

where N is the number of digitized snapshots.

Further, the coordinates of the signals are estimated by means of the Multiple Signal Classification (MUSIC) method, which is eigenvalue-based and overcomes the resolution according to the Rayleigh criterion, i.e., less than the width of the main lobe of the array pattern [24]:

$$P_{\mathrm{MU}}(\theta) = \frac{1}{\left|\vec{\mathbf{a}}^{H}(\theta)\,\mathbf{E}_N\mathbf{E}_N^{H}\vec{\mathbf{a}}(\theta)\right|} \tag{33}$$

where $\mathbf{E}_N$ is the noise subspace matrix. At the final stage, the vector of the weight coefficients is calculated as [25]:

$$\vec{\mathbf{w}}_{\mathrm{MV}} = \frac{\mathbf{R}_{i+n}^{-1}\vec{\mathbf{a}}(\theta_0,\phi_0)}{\vec{\mathbf{a}}(\theta_0)^{H}\mathbf{R}_{i+n}^{-1}\vec{\mathbf{a}}(\theta_0,\phi_0)}, \tag{34}$$

Further, the study is based on modeling to estimate the range of propagation of wireless telecommunication signals in the troposphere layers. The maximum range is selected to be 150 km, and the resolution is 500 m in all cases. Obviously, in order to track all the rays from the transmitter arriving at the receiving array, it is necessary to trace absolutely the entire range of elevation angles (a brute-force search). An expression that displays the limit values for the elevation angles of propagation of a radio wave in an air tropospheric waveguide is known [19]:

$$\varphi_{\min,\,\max} = \pm\sqrt{2\left(\frac{1}{n(0)}\frac{dn}{dh} - \frac{1}{R_0}\right)(h_t - \delta)}, \tag{35}$$

where δ is the thickness of the trapping layer.

In experiments, it is supposed that the transmitter antenna is deployed at a height of 200 m. The probability of a bit error rate is estimated as the ratio of the number of erroneous bits to their total number, and binary phase shift key (BPSK) is utilized as a signal with a speed of 1 Mbit/s. The power of the transmitter is equal to 1 W, and the noise power of the VHF band is $1.7 * 10^{-13}$ W [26]. The simulation flow is outlined in Fig. 5.

5.1. Experiment 1: An Idealized Surface Tropospheric Duct

In this experiment, a surface waveguide is studied. Accordingly, the modified refraction profile is shown in Fig. 6. The transmitter antenna is supposed to be at a height of 200 m. Fig. 6 shows the negative slope of the level $-100\,M$-values km^{-1} from 0 m up to 350 m and then the slope 117 M-values km^{-1}.

Next, Fig. 7(a) shows the distribution of the electromagnetic field depending on the distance from the transmitter and the height above the Earth's surface. The calculation was carried out according to the apparatus of the parabolic equation and the

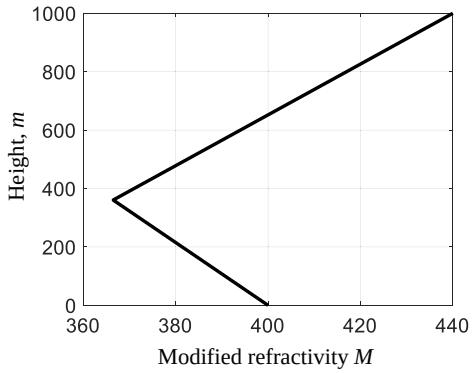

FIGURE 6. Modified refractivity M-profile of simple surface duct.

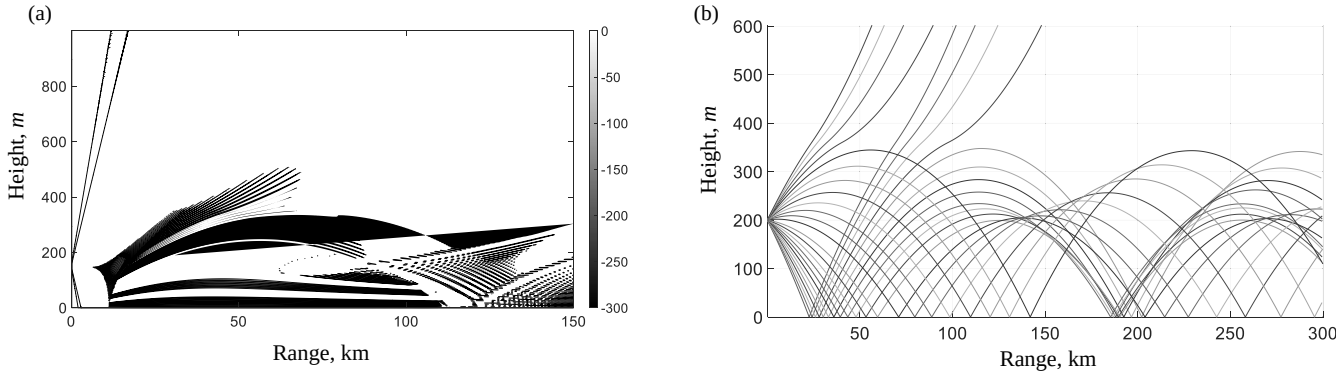

FIGURE 7. Field characteristics: (a) Propagation factor, dB; (b) Rays propagating in the lower layers of the tropospheric duct.

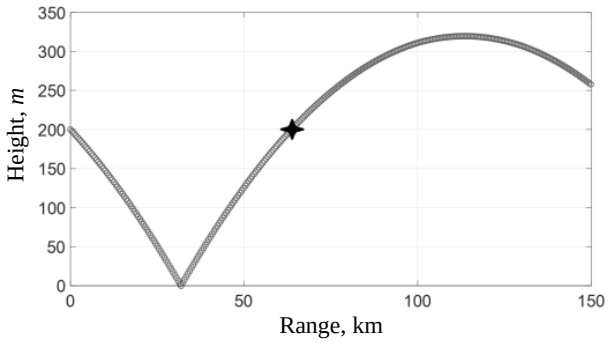

FIGURE 8. An example of the intersection of a ray (line) and a digital antenna array (asterisk).

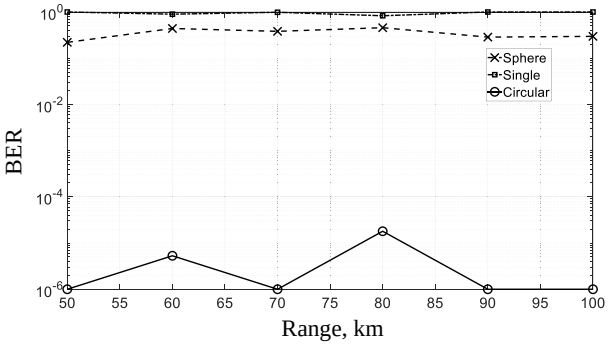

FIGURE 9. Bit error rate depending on range.

numerical Fourier splitting algorithm [27]. The refraction corresponds to the profile shown in Fig. 6. The carrier frequency is equal to 5 GHz, and a half-wave dipole is utilized as the transmitting antenna.

Figure 7(a) shows that the field distribution is uneven. Next, Fig. 7(b) shows that the rays are reflected from the upper boundary of the trapping layer, after which they reach the surface of the Earth, from which they are reflected again. This process continues to the receiving array with attenuation, as shown in Fig. 7. Next, Fig. 8 shows one of these beams, which crosses the receiving digital antenna array.

The curves of bit error rate depending on the geometry of antenna array and the range from 50 km to 100 km to the transmitter are depicted in Fig. 9. Here the attenuation of the signals traveling through the duct is about -130 dB.

The graphs in Fig. 9 indicate that the circular antenna array has the lowest bit error rates., i.e., 10^{-6}. If the hemispherical array geometry or the directional antenna is used on the receiving side, then the probability of bit error rates is equal to 0.3 and 0.8, respectively.

5.2. Experiment 2: Idealized Tropospheric S-Shaped Duct

Now all these methods are applied to the idealized surface of the S-shaped duct, characterized by the M-profile shown in Fig. 10. The profile starts with tilt 117 M-values km^{-1} for the lowest

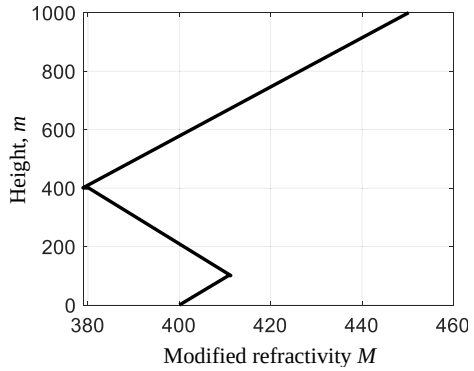

FIGURE 10. Modified refractivity M-profile of simple S-shaped duct.

100 m, and then changes to -100 M-values km^{-1} up to 400 m, after which it returns to 117 M-values km^{-1}.

Further, in Fig. 11 the parameters of the electromagnetic field distribution in accordance with the profile of the modified refractive index shown in Fig. 10 are demonstrated.

Figure 11(a) shows that the propagation factor is 15 dB higher at a transmitter height of 200 m than a wave in free space. Additionally, the curves of the loss values depending on the distance between the transmitter and the receiving array are shown, from which it can be concluded that an electromagnetic wave inside a tropospheric waveguide loses 15–20 dB less power than a radio signal in free space or outside the trapping layer. Additionally, the ray trajectories for the refraction index under consideration are given in Fig. 11(b). It can be seen that the rays can both re-reflect from the Earth's surface and bend at the lower and upper boundaries of the troposphere layers.

It can be seen from the graphs in Fig. 12 that the circular array allows obtaining the least number of errors. Thus, from Figs. 10 to 12, it can be said that radio signals at a frequency of 5 GHz can reach a receiver located more than 100 km from the transmitter, while having a bit error rate within 10^{-6}, which is acceptable for most modern wireless telecommunication systems.

5.3. Experiment 3: Idealized Elevated Duct

Consider an idealized elevated duct. The corresponding M-profile is shown in Fig. 13. The modified M-profile starts with tilt 117 M-values km^{-1} for the first 250 m, and then it changes to -100 M-values km^{-1} up to 400, and finally returns to 117 M-values km^{-1}. The antenna height is also 300 m within the trapping layer.

Figure 13 shows that the duct in this case is raised and does not touch the surface of the Earth. Next, the characteristics of this type of atmosphere are depicted in Fig. 14.

From Fig. 14(a) it can be seen that an electromagnetic wave at a frequency of 5 GHz and a transmitter height of 300 m will have greater power than free space propagation. In addition, from Fig. 14(a) it becomes obvious that the advantage of propagation inside a tropospheric waveguide is manifested at distances over 100 km, since in this case the loss is 20 dB less than in free space. Additionally, typical ray trajectories for the elevated waveguide are shown in Fig. 14(b).

The curves of the probability of bit error rates depending on the distance between the transmitter and the receiving array are presented in Fig. 15. It is worth nothing that the array is located at an altitude of 300 m inside the elevated tropospheric waveguide.

It can be seen from the graphs in Fig. 15 that low bit error values can be achieved via the circular antenna array, i.e., 10^{-6}, compared with the hemispherical geometry and the simple directional emitter, which have 0.3 and 0.9, respectively.

The behavior of the circular antenna array can be explained as follows. First, a histogram of the elevation coordinates of the arrival of the signal at the aperture of the digital antenna array after passing through the tropospheric waveguide is presented in Fig. 16. In this case, the simple surface duct from Fig. 6 is considered in the first glance.

It can be seen from Fig. 16 that most of the distribution is concentrated in the area of the elevation equal to 90°. This is a result of the beam spreading over several hundred kilometers and not exceeding hundreds of meters in height within the trapping layer. Thus, the difference between the horizontal and vertical components of the propagation path is about a thousand times.

The direction-of-arrival estimation algorithm MUSIC and the minimum variance distortionless response algorithm, which is an optimal beamformer, are evaluated statistically. The research is studied depending on the elevation coordinate. The signal-to-noise-plus-interference ratio (SNIR) at the antenna array output is estimated for the beamformer using the following formula [28]:

$$\text{SNIR} = \frac{\vec{\mathbf{w}}^H \mathbf{R}_{ss} \vec{\mathbf{w}}}{\vec{\mathbf{w}}^H \mathbf{R}_{i+n} \vec{\mathbf{w}}} \tag{36}$$

where $\mathbf{R}_{ss}$ is the spatial matrix of the useful signal, and $\mathbf{R}_{i+n}$ is the spatial interference and noise matrix.

The standard error (RMSE) of the MUSIC is defined as follows:

$$\text{RMSE}_\theta\left(\phi_m, \theta_m\right) = \frac{1}{L-1}\sqrt{\sum\nolimits_{l=1}^{L}\left(\theta - \hat{\theta}_l\right)^2} \tag{37}$$

where L is the number of tests, and "$\hat{}$" is the estimation of the spatial coordinate.

In addition, the Cramer-Rao lower bound is utilized in order to assess the considered antenna arrays analytically. Thus, the covariance matrix of error of 3D direction-of-arrival (DOA) estimation:

$$\mathbf{B}_{\text{STO}} = \frac{\sigma^2}{2N}\Re\left[\text{Tr}\left\{\begin{bmatrix}\Lambda_1 & \Lambda_2\\ \Lambda_3 & \Lambda_4\end{bmatrix} \circ \begin{bmatrix}\Xi & \Xi\\ \Xi & \Xi\end{bmatrix}^T\right\}\right]^{-1} \tag{38}$$

where $\mathbf{\Lambda}_1 = \mathbf{D}_\theta^H \mathbf{P}_A^\perp \mathbf{D}_\theta$, $\mathbf{\Lambda}_2 = \mathbf{D}_\theta^H \mathbf{P}_A^\perp \mathbf{D}_\varphi$, $\mathbf{\Lambda}_3 = \mathbf{D}_\varphi^H \mathbf{P}_A^\perp \mathbf{D}_\theta$, $\mathbf{\Lambda}_4 = \mathbf{D}_\varphi^H \mathbf{P}_A^\perp \mathbf{D}_\varphi$, $\Xi = \mathbf{S}\mathbf{A}^H \mathbf{R}^{-1} \mathbf{A}\mathbf{S}$. Define $\mathbf{D}_\theta$ and $\mathbf{D}_\varphi$ [29]:

$$\mathbf{D}_{\theta,\phi} = \left[\left.\frac{\partial \vec{\mathbf{a}}\left(\theta_1, \phi_1\right)}{\partial \eta}\right|_{\eta=\theta_1,\phi_1}, \ldots, \left.\frac{\partial \vec{\mathbf{a}}\left(\theta_d, \phi_d\right)}{\partial \eta}\right|_{\eta=\theta_d,\phi_d}\right] \tag{39}$$

In the following figures, the curves of expressions (37), (38), (39) are shown. Here, the initial value of the signal-noise ratio

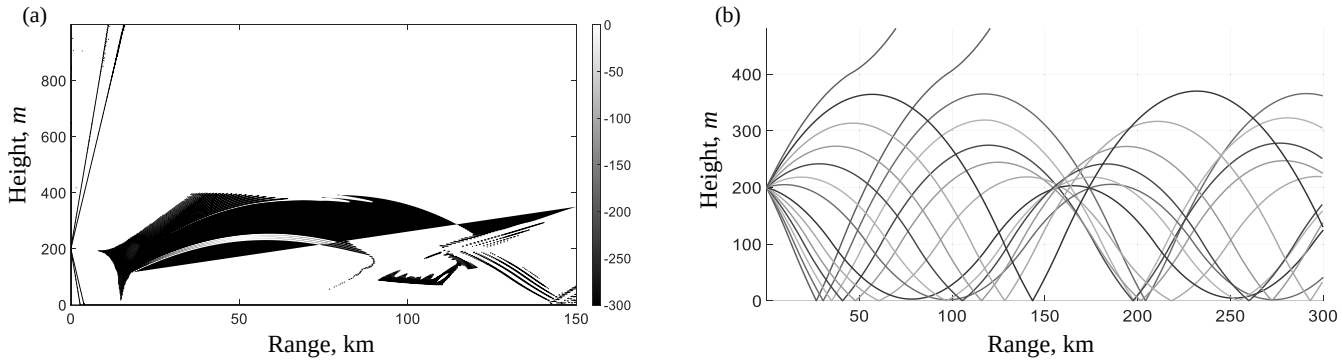

FIGURE 11. Field characteristics: (a) Propagation factor, dB; (b) Rays propagating in the lower layers of the tropospheric duct.

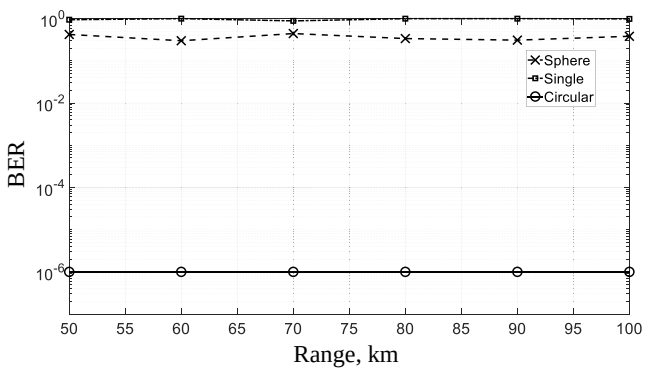

FIGURE 12. Bit error rate depending on range.

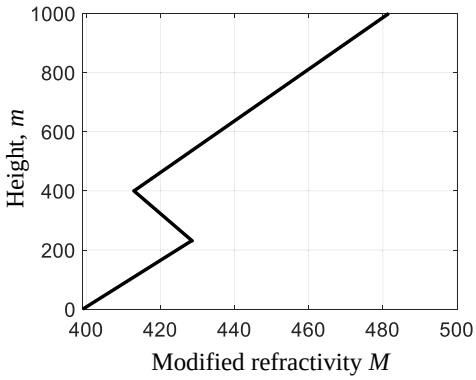

FIGURE 13. Modified refractivity M-profile of duct.

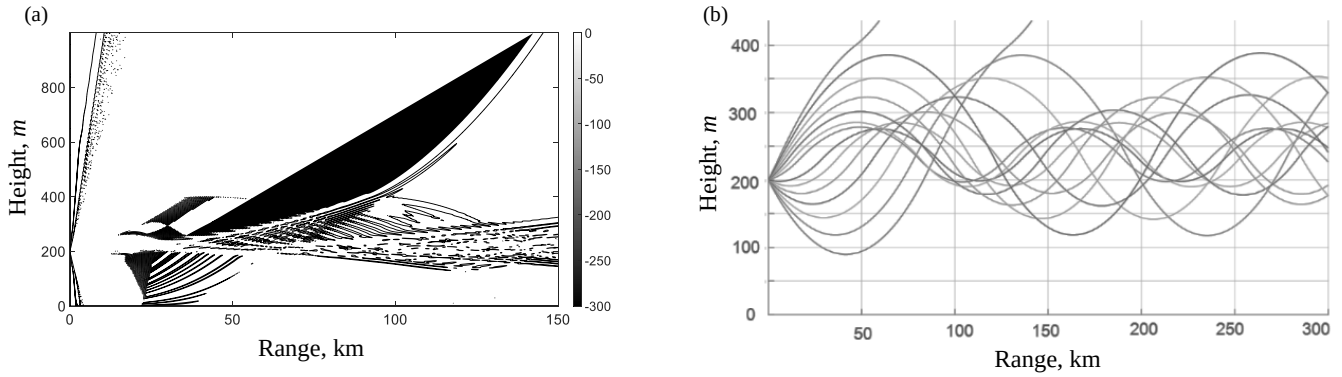

FIGURE 14. Field characteristics: (a) Propagation factor, dB; (b) Rays propagating in the layers of the tropospheric duct.

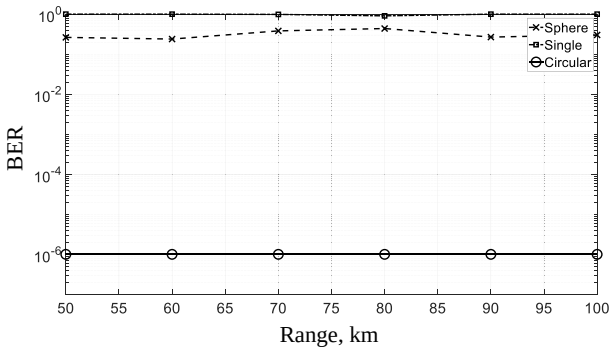

FIGURE 15. Bit error rate depending on range.

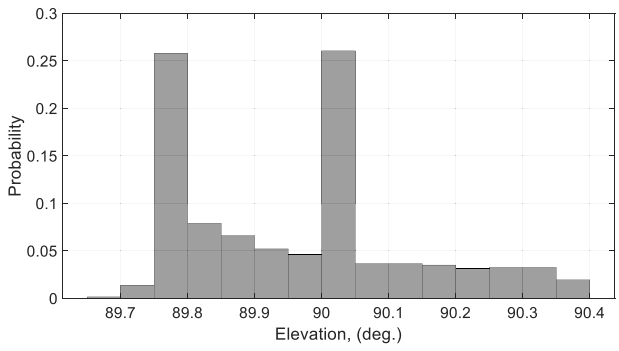

FIGURE 16. Histogram of the elevation coordinates of the signal traveling through the simple duct.

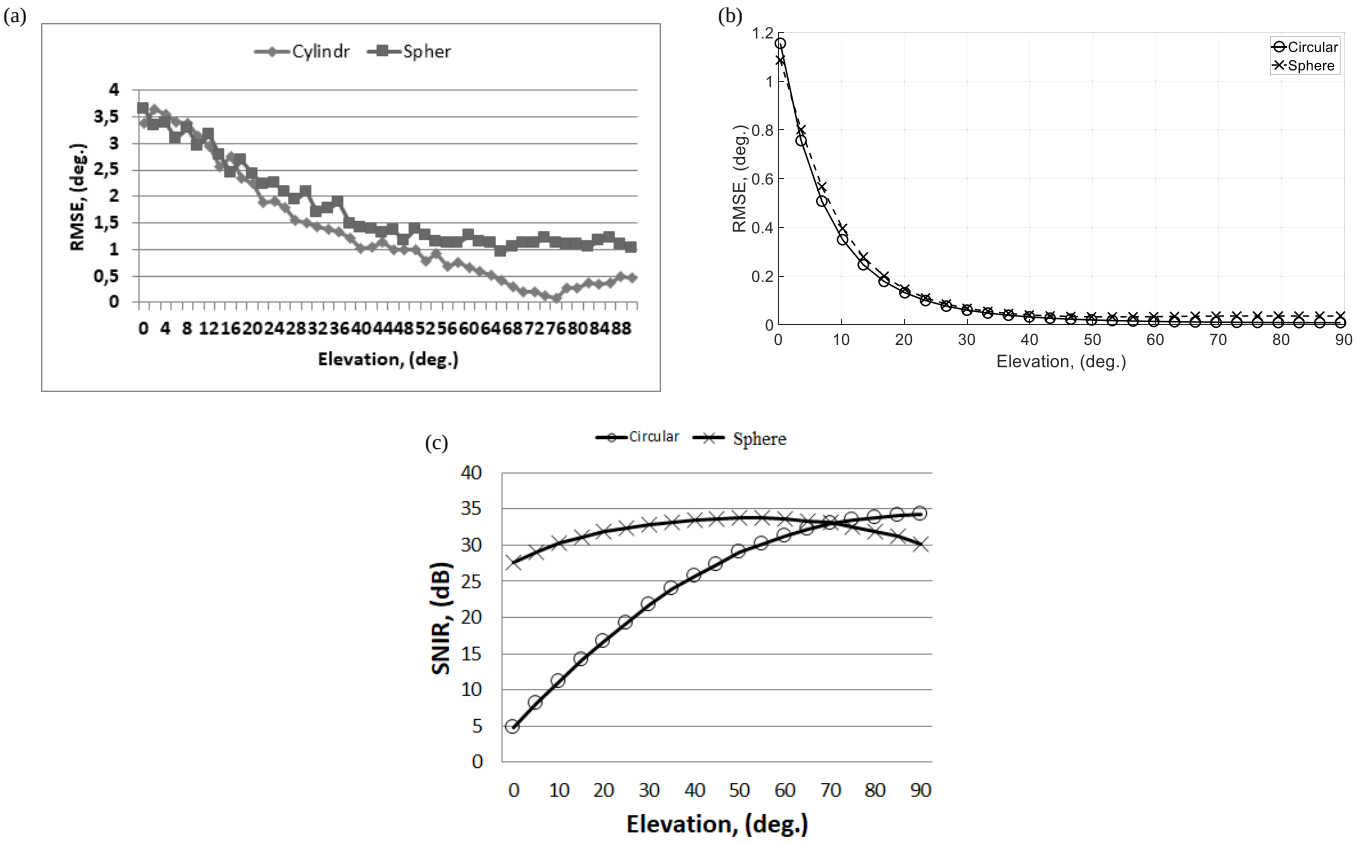

FIGURE 17. Characteristics of antenna arrays depending on the elevation: (a) MUSIC, (b) Cramer-Rao lower bound and (c) SNIR of the beamformer.

is equal to 0 dB, and the elevation coordinate is altered from 0° to 90°.

It can be seen from Fig. 17 that the accuracy of the circular antenna array is higher than that of the hemispherical one in the area of the elevation coordinate equal to 90°. At the same time, the circular antenna array also has higher values of SNIR under ideal conditions, i.e., it is assumed that the coordinates of the useful signal and interference are known. The circular antenna array is more advantageous for communication through a tropospheric waveguide because of the improved accuracy of direction-of-arrival estimates and increased SNIR after beamforming.

5.4. Experiment 4. Waveguide with Random Refraction

The physical processes in the troposphere are complex enough [30]. Thus, it is important to consider a tropospheric waveguide with a random refraction index, which is more natural. It is proposed to use the following model of probability density $f(x)$ and cumulative distribution function $F(x)$ [31]:

$$f(x) = \frac{c}{2}\exp\left(c\left(x-\mu\right)\right), \quad -\infty < x < x_p \tag{40}$$

$$f(x) = \frac{1}{2\sqrt{2\pi}}\exp\left(\frac{\left(x-\mu\right)^2}{2\sigma^2}\right), \quad x_p < x < \infty \tag{41}$$

$$F(x) = \frac{1}{2}\exp\left(c\left(x-\mu\right)\right), \quad -\infty < x < x_p \tag{42}$$

$$F(x) = \frac{1}{2}\left[1 + erf\left(\frac{\left(x-\mu\right)}{\sigma\sqrt{2}}\right)\right], \quad x_p < x < \infty \tag{43}$$

where μ is the average value of the refractive gradient, and σ is the standard deviation of the refractive gradient.

$$c\sigma = \frac{\ln\left(2P\right)}{\sqrt{2}\,\mathrm{inverf}\left(2P-1\right)} \tag{44}$$

where $P = (x_p)$.

It is obvious from formulas (41)–(45) that it is necessary to obtain values from a non-standard statistical distribution. This can be fulfilled using one of the algorithms: Ziggurat [32] and inverse transformation of the distribution and rejection sampling [33].

5.4.1. Rejection Sampling

Suppose that it is needed to sample from a distribution $f(x)$, from which it is difficult or impossible to select directly, but instead there is a simpler distribution $q(x)$, from which it is easy to sample. The idea of rejection sampling is to take $q(x)$ and apply some rejection/acceptance criteria so that the samples that were accepted are distributed according to $f(x)$. The general criterion for accepting samples from $x \sim q(x)$ is based on the ratio of the target distribution to the envelope distribution, i.e., samples are accepted if:

$$\frac{f(x)}{cq(x)} > u \tag{45}$$

where $u \sim \text{Unif}(0, 1)$, and rejected otherwise.

A graph of samples from the statistical distribution (41)–(44) obtained according to the rejection sampling algorithm is depicted in Fig. 18 below.

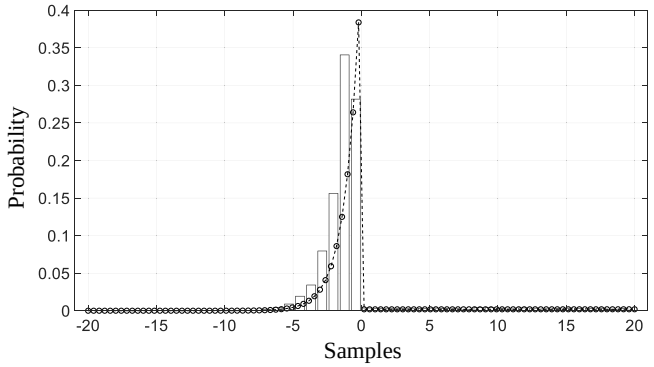

FIGURE 18. "The dashed curve" is the theoretical distribution of (40)–(41), "the blank rectangles" are histograms of the distribution of samples, obtained by the rejection sampling algorithm.

The graphs in Fig. 19 below show the curve of the modified refractivity M with random values from the distribution (40)–(43). Moreover, Fig. 20 depicts some rays that have passed through the random tropospheric duct.

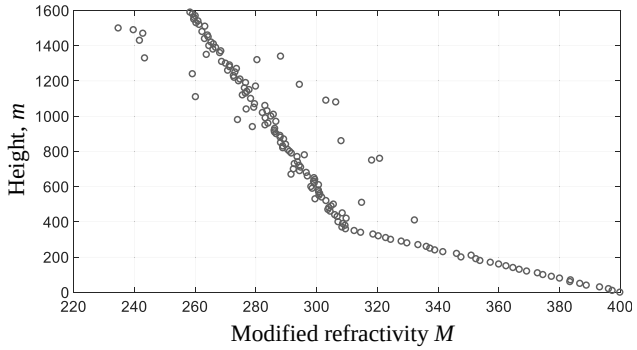

FIGURE 19. Random modified refractivity.

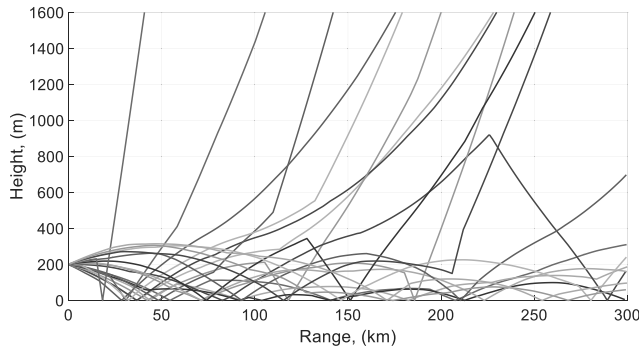

FIGURE 20. The rays through the random duct.

Comparing Fig. 20 with Fig. 7(b), it can be said that more rays began leaving the random duct after traveling through it. The trajectory of the rays became sharper and more curved.

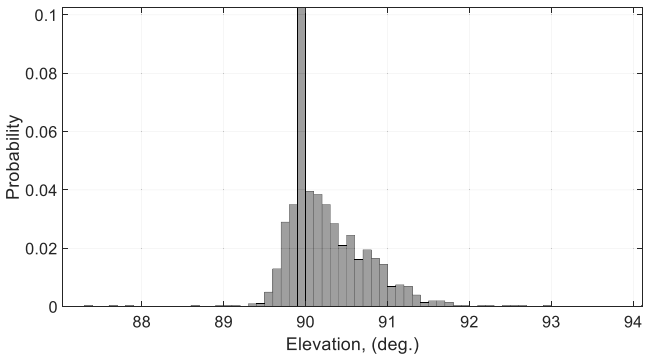

FIGURE 21. Histogram of the elevation coordinates of the signal traveling through the random duct.

Consider the distribution of the elevation coordinates of the rays after traveling through the random tropospheric duct.

Having compared Fig. 21 with Fig. 16, it is worth nothing that the elevation coordinates after the random tropospheric waveguide have a larger distribution. If earlier they were concentrated around 90°, then now they reach 91° and even 92° and further. In Figure 22, a graph of the probability of a bit error rate when transmitting a radio signal over a tropospheric channel with random values of the refraction gradient is shown.

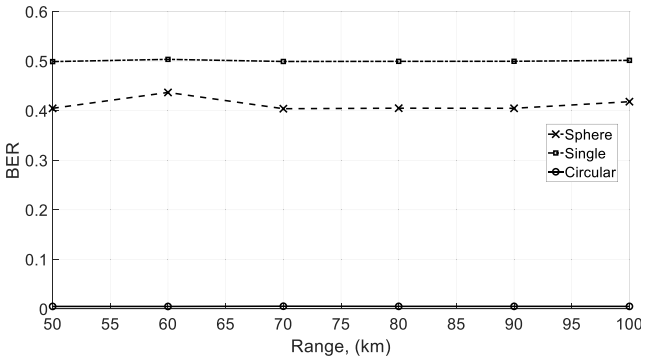

FIGURE 22. Bit error rate after traveling through the random duct.

After viewing Fig. 22 it can be said that the circular antenna array allows obtaining the least number of bit error rate when communication is linked via a random duct.

6. CONCLUSIONS

A tropospheric waveguide in the lower layers of the atmosphere takes place if there is a change in the modified refraction index from the maximum value at the ground surface to the minimum at a certain altitude. In order to simulate signal transmission via a tropospheric duct and then spatial processing correctly, several sequential means were used: ray-tracing, losses calculation taking into account refraction index, antenna height, carrier frequency, etc. Additionally, modified refractive index with random values was studied. After DOA estimation and digital beamforming, the probability of a bit error rate was estimated. The circular shape of the antenna array with spatial processing has been suggested to be used in the tropospheric waveguide.

ACKNOWLEDGEMENT

The study was funded by Russian Science Foundation according to the research project No. 23-21-00125, https://rscf.ru/project/23-21-00125/.

REFERENCES

[1] Schelleng, J. C., C. R. Burrows, and E. B. Ferrell, "Ultra-short-wave propagation," *Proceedings of the Institute of Radio Engineers*, Vol. 21, No. 3, 427–463, 1933.

[2] Anderson, K. D., "Radar measurements at 16.5 GHz in the oceanic evaporation duct," *IEEE Transactions on Antennas and Propagation*, Vol. 37, No. 1, 100–106, Jan. 1989.

[3] Dinc, E. and O. B. Akan, "Beyond-line-of-sight communications with ducting layer," *IEEE Communications Magazine*, Vol. 52, No. 10, 37–43, Oct. 2014.

[4] Woods, G. S., A. Ruxton, C. Huddlestone-Holmes, and G. Gigan, "High-capacity, long-range, over ocean microwave link using the evaporation duct," *IEEE Journal of Oceanic Engineering*, Vol. 34, No. 3, 323–330, Jul. 2009.

[5] Lindquist, T., "Wave propagation models in the troposphere for long-range UHF/SHF radio connections," M.S. thesis in Engineering Physics, Karlstad University, Karlstad, Sweden, 2020.

[6] Gao, Y., Q. Shao, B. Yan, Q. Li, and S. Guo, "Parabolic equation modeling of electromagnetic wave propagation over rough sea surfaces," *Sensors*, Vol. 19, No. 5, 1252, 2019.

[7] Zeng, Y., U. Blahak, M. Neuper, and D. Jerger, "Radar beam tracing methods based on atmospheric refractive index," *Journal of Atmospheric and Oceanic Technology*, Vol. 31, No. 12, 2650–2670, 2014.

[8] Zhao, X.-F., S.-X. Huang, and Z. Sheng, "Ray tracing/correlation approach to estimation of surface-based duct parameters from radar clutter," *Chinese Physics B*, Vol. 19, No. 4, 049201, 2010.

[9] Feng, G., J. Huang, and M. Yi, "General formulas of effective Earth radius and modified refractive index," *IEEE Access*, Vol. 9, 115 068–115 076, 2021.

[10] Zhao, X.-F. and S.-X. Huang, "Refractivity estimations from an angle-of-arrival spectrum," *Chinese Physics B*, Vol. 20, No. 2, 029201, 2011.

[11] Valtr, P. and P. Pechac, "Analytic tropospheric ray-tracing model for constant refractivity gradient profiles," in *2006 First European Conference on Antennas and Propagation*, 1–4, 2006.

[12] International Telecommunication Union, Radiocommunication Sector of ITU-R, "Recommendation ITU-R P.834-6. Influence of tropospheric refraction on propagation of radio waves," Tech. Rep., 2007.

[13] International Telecommunication Union, Radiocommunication Sector of ITU-R, "Recommendation ITU-R P.453-14. The radio refractive index: Its formula and refractivity data," Tech. Rep., 2019.

[14] Hartree, D. R., J. G. L. Michel, and P. Nicolson, "Practical methods for the solution of the equations of tropospheric refraction," in *Meteorological Factors in Radio-wave Propagation*, 127–168, The Physical Society, 1947.

[15] Lentovich, M. A. and V. A. Fok, "Solution of propagation of electromagnetic waves along the Earth's surface by the method of parabolic equations," *Journal of Physics-USSR*, Vol. 10, 13–23, 1946.

[16] Nilsson, M., "Radio-wave propagation modelling over rough sea surfaces and inhomogeneous atmosphere," M.S. thesis in Engineering Physics, Karlstad University, Karlstad, Sweden, 2021.

[17] Levy, M., *Parabolic Equation Methods for Electromagnetic Wave Propagation*, 336, IEE, London, 2000.

[18] Ozgun, O., "Recursive two-way parabolic equation approach for modeling terrain effects in tropospheric propagation," *IEEE Transactions on Antennas and Propagation*, Vol. 57, No. 9, 2706–2714, 2009.

[19] Dinc, E. and O. B. Akan, "Channel model for the surface ducts: Large-scale path-loss, delay spread, and AOA," *IEEE Transactions on Antennas and Propagation*, Vol. 63, No. 6, 2728–2738, Jun. 2015.

[20] Zhao, X.-F. and S.-X. Huang, "Refractivity estimations from an angle-of-arrival spectrum," *Chinese Physics B*, Vol. 20, No. 2, 029201, 2011.

[21] Zhao, X. and P. Yang, "A simple two-dimensional ray-tracing visual tool in the complex tropospheric environment," *Atmosphere*, Vol. 8, No. 2, 35, 2017.

[22] Balanis, C. A. and P. I. Ioannides, *Introduction to Smart Antennas*, 174, Morgan & Claypool Publishers, San Francisco, 2007.

[23] Fortunova, N. A., I. W. Peshkov, A. N. Kalabukhov, and Y. B. Nechaev, "The influence of directive elements of conformal and planar antenna arrays on the performances of azimuth-elevation DOA-estimation methods with super resolution," in *2019 Systems of Signal Synchronization, Generating and Processing in Telecommunications (SYNCHROINFO)*, 1–7, Russia, 2019.

[24] Schmidt, R., "Multiple emitter location and signal parameter estimation," *IEEE Transactions on Antennas and Propagation*, Vol. 34, No. 3, 276–280, Mar. 1986.

[25] Shiu, W. Y., "Noniterative digital beamforming in CDMA cellular communications systems," Master thesis, Queen's University, Kingston, Ontario, Canada, Nov. 1998.

[26] Nechaev, Y. B. and I. W. Peshkov, "Simulation of digital and analog spatial filtering of VHF signals in channel with losses due to multipple diffraction," in *2022 Systems of Signals Generating and Processing in the Field of on Board Communications*, 1–5, 2022.

[27] Ozgun, O., G. Apaydin, M. Kuzuoglu, and L. Sevgi, "PETOOL: MATLAB-based one-way and two-way split-step parabolic equation tool for radiowave propagation over variable terrain," *Computer Physics Communications*, Vol. 182, No. 12, 2638–2654, 2011.

[28] Van Veen, B. D. and K. M. Buckley, "Beamforming: A versatile approach to spatial filtering," *IEEE ASSP Magazine*, Vol. 5, No. 2, 4–24, Apr. 1988.

[29] Nechaev, Y., I. Peshkov, and N. Fortunova, "Evaluation and minimization of Cramer-Rao bound for conformal antenna arrays with directional emitters for DOA-estimation," *Progress In Electromagnetics Research C*, Vol. 90, 139–154, 2019.

[30] Grabner, M. and V. Kvicera, "Atmospheric refraction and propagation in lower troposphere," in *Electromagnetic Waves*, IntechOpen, London, United Kingdom, 2011.

[31] Brussaard, G., *Handbook on Radiometeorology*, International Telecommunication Union, Switzerland, 1996.

[32] Marsaglia, G. and W. W. Tsang, "The ziggurat method for generating random variables," *Journal of Statistical Software*, Vol. 5, No. 8, 1–7, 2000.

[33] Robert, C. P. and G. Casella, *Monte Carlo Statistical Methods*, 645, Springer-Verlag, Berlin, Heidelberg, 2010.